The *in vacuo* release of Ar from minerals: 3. The degassing of He, Ne, Ar, Kr and Xe from irradiated apatite

Igor M. Villa[1,2], Sergio Andò[1], Giancarlo Capitani[1], Massimiliano Clemenza[3], Roberto Conconi[1], Lucia Galimberti[1], Massimo Oddone[4]

[1] Dipartimento di Scienze dell'Ambiente e della Terra, Università di Milano Bicocca, 20126 Milano, Italy

[2] Institut für Geologie, Universität Bern, 3012 Bern, Switzerland

[3] Istituto Nazionale di Fisica Nucleare, Università di Milano Bicocca, 20126 Milano, Italy

[4] Dipartimento di Chimica Generale, Università di Pavia, Pavia, Italy

Abstract

A 200 mg shard of Durango fluorapatite was stepheated after neutron irradiation. It contained radiogenic ^{4}He from natural U decay and artificially produced rare gase isotopes: ^{20}Ne from F, ^{37}Ar from Ca, ^{38}Ar from Cl, ^{80}Kr and ^{82}Kr from Br, ^{128}Xe from I, and ^{131}Xe from Ba. The ^{4}He release rate was compared with that from an unirradiated aliquot.

He was expected, and observed, to degas at the lowest furnace temperatures, with a degassing peak around 1000 °C and nearly complete exhaustion by 1200 °C. Ne followed a bimodal degassing pattern, with a peak at 1178 °C and a higher one at 1406 °C. Ar degassing showed the same peaks. Kr and Xe were both released in a single, major burst between 1360 and 1460 °C.

The two Xe isotopes 128 and 131, produced from I and Ba, respectively, followed exactly the same degassing pattern. The crystallographic site of the target element had no control on the successive movement of the irradiation-produced rare gas atom after it had recoiled during irradiation and before it exited the crystal by crossing a large number of unit cells.

The He release from the irradiated and unirradiated aliquots gave two nearly overlapping alignments in the Arrhenius diagram at intermediate temperatures between 500 and 1100 °C. The two slopes are indistinguishable at the 1 sigma level and yield an average activation energy of 60±6 kJ/mole. In the same temperature interval, all five rare gases showed parallel trends with an activation energy around 60 kJ/mole and diffusion constants decreasing from He to Xe by about 3-4 orders of magnitude. Arrhenian trajectories for Kr and Xe sharply steepen, with a degassing rate about 2000-5000 times higher than at intermediate temperatures, and merge at 1290 °C, with an activation energy of ca. 1600 kJ/mole. The high-T modes of the Ar and Ne release also fall on the same steep Arrhenius line, with indistinguishable diffusivities as Kr and Xe. This break in

Arrhenius slope and the merger of four trajectories that were well separated below 1200 °C indicate a major, energetically very costly structural reordering of apatite around 1300 °C.

The structural reordering was looked for, and well documented, by three mineralogical techniques: Raman spectroscopy, X ray diffractometry, and microchemical analysis by laser induced breakdown spectroscopy. Complete loss of structural fluorine heavily modified the apatite structure. Complete outgassing of Ne, Ar, Kr and Xe was only achieved after the defluorination reaction and attending structural collapse.

Key words: Ar diffusion, noble gas diffusion, apatite degassing, crystal structure modification

Introduction

An unsolved issue with gas release studies is the role of the atomic radius in enabling the transport of rare gas atoms through the mineral structure. It was established (e.g. Cherniak at al., 1997a,b) that diffusion of tri- and tetravalent cations strongly depends on the ionic radius, whereby the activation energy is constant and only the pre-exponential factor (the jump frequency) varies. It is therefore expected that *bona fide* diffusion of rare gases should obey the same law. On the other hand, Ar release from micas is controlled by a structural breakdown (Villa, 2021, and references therein), and structural rearrangements strongly affect the Ar release also from feldspar (Kung and Villa, 2021). The present experiment is designed to assess the relative roles of diffusion and of structural breakdown in the release of the five rare gases, whose ionic radii are very different, from apatite, a nominally anhydrous mineral containing measurable amounts of all five when neutron-irradiated.

Analytical methods

Rare gas release was studied on a crystallographically coherent, roughly cubic fragment hereafter referred to as Fragment A, of the Durango apatite, donated by P. Vermeesch. Fragment A was irradiated at the Triga Research Reactor, University of Pavia, carefully avoiding Cd shielding, which would suppress the production of rare gas isotopes from halogens. Another small roughly cubic fragment of the same crystal, Fragment B, was analyzed unirradiated, in order to compare the He degassing rate before and after irradiation. The equivalent grain radii were a_{irr} = 2.47 mm and a_{unir} = 0.67 mm for the irradiated and unirradiated fragment, respectively. For the subsequent mineralogical analyses a 200 µm thick slice, perpendicular to the c axis, of the Durango apatite was microsawed from a different euhedral crystal.

Stepwise heating and rare gas analyses were performed at Dipartimento di Scienze dell'Ambiente e della Terra at Università di Milano Bicocca, Italy, hereafter DISAT, using the same protocol and apparatus as described by Villa (2021). It is important to point out that in the reverse geometry furnace at DISAT the cylindrical heating element surrounds the bottom-up Ta crucible, into which a Mo liner is inserted from the bottom, completely enclosing the content of the Mo liner from all sides. In this experiment the temperature was never reduced between heating steps, each of which lasted between 10 and 155 min. The furnace temperature was calibrated by the melting points of

pure metal wires between 318 and 1440 °C (Pb, Al, Ag, Cu, Be, Ni), held at constant temperature for 15 minutes.

He and Ne were measured sequentially in a single gas introduction, performed while Ar, Kr and Xe were retained onto charcoal by liquid nitrogen. The possible presence of isobaric interference on the ^{20}Ne peak by doubly ionized ^{40}Ar had previously been tested by analyses of atmospheric pipettes (much gas-richer than the actual sample gas) using the same liquid nitrogen trap, and observed to be negligible. Ar was then introduced while Xe was retained on the charcoal by an ethanol-solid CO_2 mixture. About half of the Kr was introduced together with Ar, but not analyzed due to the probable isobaric interference of the ^{40}Ar dimer on the ^{80}Kr peak. Trapping Kr only partially by this protocol provides relative Kr outgassing rates reliably; absolute Kr outgassing rates could be inferred by calibrating the ratio of the proportion of Kr introduced with Ar to that introduced with Xe. The heavy rare gases, Xe and the remaining Kr, were then introduced together into the mass spectrometer by warming the charcoal to ca. 120 °C and analyzed sequentially. The results for all five gases are presented in Supplementary Table S1.

The mineralogical analyses made use of a thin, unirradiated hexagonal slice, which was divided in two halves, referred to as fragments C and D, having a rhomboidal shape with the longest side of 5 mm. Fragment C was analyzed, non-destructively, by Raman microprobe and by XRD. It was then stepheated, unirradiated, to the same temperatures as the irradiated Fragment A. During the stepheating, He and Ne were also collected; the He release pattern of C closely reproduced that of A. The purpose of analyzing Ne in fragment C was controlling the efficiency of the Ar trapping described above, ascertaining that that no $^{20}(Ar^{2+})$ was detectable in any heating step and that no spurious non-atmospheric ^{20}Ne excess could have biased the fluorine-derived $^{20}Ne_F$ measurements in irradiated Fragment A. After the stepheating, Fragment C was again analyzed by Raman microprobe in the same position and setup as when it was unheated. After the Raman analysis its composition was analyzed by LIBS and by XRD. Unheated fragment D was kept in reserve.

Raman spectroscopy was performed at DISAT using a Micro-Raman Renishaw - inVia spectrometer (Andò and Garzanti, 2013). Results are shown in Fig. 4.

The X-ray diffractometry (XRD) analysis was performed at DISAT using a PANalytical X'Pert PRO PW3040/60 diffractometer. Results are shown in Fig. 5.

The in situ chemical microanalysis was performed by Laser Induced Breakdown Spectroscopy (LIBS) at Dipartimento di Fisica, Università di Milano Bicocca, using a Thermo-Fisher Niton Apollo Handheld LIBS Analyzer.

Results and discussion

The He degassing rate is presented in Figure 1. The degassing of the irradiated Fragment A does not coincide with that of the unirradiated Fragment B, which occurs at lower *T*. This may have two, mutually not exclusive, causes. (i) The two degassing routines are not identical. Heating of Fragment B started at 309 °C and resulted in rapid He outgassing, and reached the degassing peak in step 9 (778 °C) after 4440 s; Fragment A was heated starting at 428 °C and reached the peak in step 9 (880 °C) after 14760 s. Thus any transport mechanism that has a non-thermally-activated component will make the two degassing rates not comparable. (ii) The irradiated fragment has a larger number of irradiation-produced defects, and therefore (see below) starts with a low degassing rate and a higher activation energy. The two trajectories merge at 455 °C. Since merging Arrhenius trajectories have been argued to represent a structural modification (Villa, 2021), this may be the temperature at which both natural tracks (alpha recoil and U fission) and artificial irradiation tracks are annealed. A similar effect could be the explanation for the observations by Farley (2000, p.2909). Annealing was measured by laser heating (Willett et al., 2017) at slightly lower temperatures than the present work; see the discussion on temperature calibrations below.

Figure 1a is an Arrhenius plot comparing the present data with those obtained by Wolf et al. (1996) by laser heating. Two general features are reproduced: the observation that the Arrhenius trajectory shows a break in slope, from steeper to shallower; and the absolute value of the slope at higher degassing temperature, corresponding to an activation energy of 60±6 kJ/mol (see below) in the present experiment and 56 kJ/mol in Wolf et al. (1996). Two features are different; however, even if they are briefly mentioned here, they are secondary for the present experiment, whose crux lies in the intercomparison of the five rare gases with respect to each other, obtained in the same heating step, and not in a critique of Wolf et al's (1996) use of laboratory data on He degassing to infer quantitative thermochronometric models for apatite helium dating. The differences pertain to the temperatures, at which the break in slope occurs, and at which complete outgassing of the Durango apatite is recorded. Wolf et al. (1996) state that in their experiment apatite degassing was complete below 600 °C. As the experimental setup of Wolf et al. (1996) is based on short heating by a laser beam, whereas our inverted furnace guarantees a 4π heating geometry for the present experiment, the long step durations achieved thermal equilibrium, and temperatures were calibrated by wire melting in the same geometry, it is likely that the two temperature estimates are not comparable. This is supported by our observation (Supplementary Table S1) that the most intense differential He degassing of the irradiated Fragment A of the Durango apatite occurs around 1000 °C, above the melting temperature of Ag, and is only complete about 100 °C above the melting temperature of Cu, using average heating durations of 33 min.

The very existence of a kink in the Arrhenius trajectory should be interpreted in terms of atom-scale processes, a factor not considered by Wolf et al. (1996), who only envisage macroscopic mechanisms. Lasaga (1981, p. 276) explicitly predicts Arrhenius kinks due to transitions from extrinsic to intrinsic diffusion regimes. Recent calculations by Gerin et al (2017) using Density Functional Theory confirm the suggestion by Shuster et al. (2006) that crystal defects caused by alpha particle recoil *increase* the activation energy of He transport in apatite, whereas the older literature available to Wolf et al. (1996) assumed incorrectly that the opposite was true. As alpha tracks are annealed at sufficiently high temperature, it follows that above this temperature He transport becomes less energetically costly than below it. This results in a convex Arrhenius trajectory, providing a confirmation of Lasaga's (1981) predictions.

Figure 1b compares the He degassing rate of the irradiated and the unirradiated aliquot in the temperature interval where the two stepheating experiments overlap, 500-1100 °C (*i.e.* abscissa intervals between 0.73 and 1.3). The two activation energies are 57.3±3.7 and 64.3±6.1 kJ/mol for the irradiated and unirradiated aliquot, respectively, indistinguishable at the 68% confidence level. The weighted average of the two experiments is 60±6 kJ/mol. It is possible that the neutron irradiation dose, 5.4 E17 cm^{-2} (i.e. 3.8 MWh), created less point defects than the natural dose accumulated by the untreated aliquot. This is compatible with the observation that the sum of all halogen-produced Ne+Ar+Kr+Xe nuclides in Fragment A is over 100 times lower than the measured He atoms.

The degassing rate of the heavier halogen-derived rare gas isotopes $^{20}Ne_F$ and $^{38}Ar_{Cl}$ is illustrated in Fig. 2. The differential release plot (Villa, 2021, and references therein), or DRP (Fig. 2a), shows that the $^{20}Ne_F$ release is bimodal: much of the Ne_F is released in the same steps as He, around 1000 °C, but degassing continues above the exhaustion temperature of He and a secondary burst is observed up to 1400 °C. $^{38}Ar_{Cl}$ also shows a bimodal release, at 1000 and 1400 °C, whereby the principal peak is shifted to 1400 °C. An additional Ar isotope that was analyzed and is discussed here is $^{37}Ar_{Ca}$. The DRP shows that the release patterns of the two Ar isotopes are practically identical. This similarity in the differential release of two isotopes of the same gas produced in different crystallographic sites is also observed in Xe (see below). The Arrhenius plot (Fig. 2b) compares the He trajectory (from Fig. 1) with those of $^{20}Ne_F$, $^{38}Ar_{Cl}$ and $^{37}Ar_{Ca}$. In the 500-1100 °C temperature interval $^{20}Ne_F$ and $^{38}Ar_{Cl}$ suggest an activation energy compatible with that of He release, with y-axis intercepts (D_0 values) lower than that of He by factors of 7.5 and 714, respectively. This is compatible with the quantum mechanical calculations by Gautheron et al. (2020, p. 356), which reveal that the atomic radius is not the main control on the activation energy E; in the present case, the control on diffusivity occurs via D_0, which does depend on the atomic radius. In contrast, $^{37}Ar_{Ca}$ exhibits a different behavior: it has a lower diffusivity and a higher

activation energy until 632 °C, then its trajectory coincides with that of $^{38}Ar_{Cl}$ at or near 780 °C, when the released $^{37}Ar_{Ca}$ fraction reaches 0.7 %. A possible reason for the discrepancy is the higher recoil energy of $^{37}Ar_{Ca}$ relative to $^{38}Ar_{Cl}$ (Onstott et al., 1995) produced by neutron irradiation. The potential well of the point defect thus created might be deeper in the case of $^{37}Ar_{Ca}$, resulting in a lower jump frequency and a higher activation energy in the temperature range below the annealing of the point defect, inferred to be lower or near 780 °C. As a note of caution it should be mentioned that the absolute amounts of $^{37}Ar_{Ca}$ and $^{38}Ar_{Cl}$ involved in the very low temperature Arrhenius trajectory are quite small (such that (peak height/background) ratios were <1) and may be affected by comparatively large uncertainties.

The degassing behavior of the heavy isotopes $^{80}Kr_{Br}$, $^{128}Xe_{I}$ and $^{131}Xe_{Ba}$ are illustrated in Fig. 3. Isotope $^{82}Kr_{Br}$ was also measured (Supplementary Table S1) and is numerically and graphically identical to $^{80}Kr_{Br}$. The non-atmospheric isotope ^{85}Kr was produced from ^{235}U induced fission, but was significantly above detection limit only in the 1406 °C step, in which most of the artificial Kr and Xe isotopes were released (Table S1). The Kr and Xe release patterns (Fig. 3a) are very similar to each other. In particular, the release patterns of the two Xe isotopes, produced in the very different crystallographic sites of their target elements, are identical. This is evidence that the crystallographic site did not control the successive movement of the neutron-produced Xe atom after it had recoiled during irradiation and before it left the crystal after crossing a very large number of ca. 1 nm wide unit cells. The DRP further evidences a shift of the peak of the differential gas release to the temperature range 1360-1460 °C. The Arrhenius plot (Fig. 3b) reflects this shift as a massive steepening of the trajectory; the absolute value of the activation energy is ca. 1600 kJ/mol. This degassing peak occurs over 200 °C below the melting temperature of apatite, 1618±5 °C (Bhatnagar, 1969). The mechanism of Kr and Xe degassing is clearly not the same as that of the three lighter rare gases. A similar effect had been observed for Ar and Xe by Hetherington and Villa (2007, their Fig. 6). A major structural rearrangement (cfr. Kung and Villa, 2021, and references therein) was suspected, and additional mineralogical constraints by comparing heated and unheated fragments are presented below. A defluorination reaction (expected to have an extremely costly energy budget) was suggested by a black rhomboidal print on the Mo liner at the position of Fragment A; it would result in extensive structural reordering, resembling in a more extreme way the fate of hydrous minerals upon dehydroxylation (Villa, 2021, and references therein). In the 500-1100 °C temperature range, where the light rare gases follow approximately linear Arrhenius segments, the degassing rate of Kr and Xe also follows a linear Arrhenius trajectory, about 3.5 orders of magnitude lower than that of He.

Individual atoms of Ne, Ar, Kr amd Xe in a crystal do not behave as noble gases, sometimes suggested to be "free to hover around because they make no bonds". Instead of bonding, what is

limiting their mobility is the fact that they are occluded in the mineral structure (be it in intersitial positions or in Frankel defects) and trapped there due to their atomic radius larger than the interatomic distance of the structure-forming ions. In the present work, it was observed that the large atomic radius of the four heavy rare gases effectively slows down (to different extents) their release during stepheating. It is highly inappropriate to reduce the physics of noble gas transport to Fick's Law, since Fick's Law was defined as the transport of nutrients in aqueous solutions, such that its extension outside the boundaries of its definition is likely to produce inaccurate results, as in the present case. Seeing as the mobility of noble gases in a solid crystal matrix is not accurately quantified by Fick's Law, it is mandatory to instead take into account at least two factors that forbid a linear downslope extrapolation of Arrhenius trajectories obtained in the laboratory at high temperature: (1) the atomistic behavior of defects in solids (Lasaga, 1981; Gerin et al., 2017; Gautheron et al., 2020), noting that even in a defect-free crystal structure quantum mechanics forbids rectilinear Arrhenius trajectories (Panzarini and Colombo, 1994); (2) the crystal-structural modifications that occur at discrete temperatures, such as dehydration (Villa, 2021, and references therein), phonon mode changes (Kung and Villa, 2021, and references therein), and phase transitions in general. The rate of gas release due to structural modifications is over three orders of magnitude faster than the mobility of atoms in an inert matrix (an inert matrix would be mathematically necessary if Fick's Law were an accurate description of rare gas mobility in solids). The outgassing rates of ^{80}Kr and ^{128}Xe at 1406 °C, calculated by extrapolating upslope the data between 428 and 1293 °C, should be 3.6 E-8 and 9.8 E-8 s^{-1}, respectively, whereas they are observed to be 1.5 E-4 and 1.6 E-4 s^{-1}, respectively.

The Raman spectroscopy (Fig. 4) provides hard evidence for the suspected structural modification(s). Unheated Fragment C shows a sharp peak at the 964 cm^{-1} wavenumber, which corresponds to the principal vibration mode of apatite. After heating, the same Fragment C shows a less sharp 964 cm^{-1} peak, which is interpreted as loss of crystallinity (Fig. 4a). Furthermore, the Raman map of the unheated fragment exhibits a (color-coded) heterogeneity (Fig. 4b). This observation confirms the compositional heterogeneity reported by Hasebe et al. (2004) and Marks et al. (2012). After heating, the Raman map in the same part of Fragment C shows a homogenized composition. Pre-melting, diffusional re-equilibration and mm-scale recrystallization following the suspected structural modification are all mechanisms compatible with the observation.

X-ray diffraction on unheated Fragment C has yielded a sharp 002 reflection, with a minor peak due to the 004 reflection. The analyzed material was indeed practically ideal apatite. After heating, the same fragment C has yielded a spread-out pattern with multiple peaks (Fig. 5), indicating changes of the crystal structure, supporting the Raman spectroscopy, and the probable formation of a reaction product different from apatite.

LIBS in situ analysis on heated Fragment C has documented halogen loss, with [F] below detection limit (ca. 0.01%). At least 99.7% of the initial fluorine were lost be heating. It is intuitive that the defluorinated crystal had a different cell volume from the original crystal. These structural changes were observed 200 °C below the nominal melting temperature. The delayed release of increasing amounts of Ne, Ar, and especially Kr and Xe only after a major structural reordering had already been described by McDowell (1983) for the Ar release from K-feldspar. The present results suggest that not only hydrous but also anhydrous minerals require structural collapse to be completely emptied from isotopic inheritance.

Implications for rare gas transport in geological materials

Some sort of "diffusion" always occurs, as atoms always move when $T > 0$ K. The real question that would legitimate diffusion modelling is thus not if diffusion occurs, but rather if Fick's (1855) formula, based on classical continuum mechanics, is adequate to describe the transport of atoms through a solid at all temperatures, so that downslope extrapolation to geologically relevant temperatures is always legitimate. In theory, no (Lasaga, 1981; Panzarini and Colombo, 1994; Gautheron et al., 2020). In practice, it could be argued that Fick's Law Diffusion (FLD) is sufficiently close to reality, albeit inaccurate "to some extent". The question should therefore be rephrased: "Is FLD always the one and only, mathematically invertible, transport process in all solid matrices?", or in a less rigorous formulation, "is FLD always the fastest transport mechanism, such that all other transport mechanisms play subordinate roles?". In geological systems on Earth, this is not the case. The rates of competing transport mechanisms are several orders of magnitude *faster* than FLD: recrystallization after reaction with aqueous fluids (Wood and Walther, 1982), and structural reshuffling after phase transitions (this work). A further result of this work is that at least four of the five rare gases (Ne, Ar, Kr, Xe) are not free to leave apatite unimpeded, as was commonly believed of non-bonding noble gases, and need instead a structural breakdown of the host mineral to be completely released. This guarantees isotopic inheritance in all geological situations that do not include complete recrystallization.

Conclusions

The degassing rate of the five noble gases from apatite is not compatible with Fick's Law diffusion of non-bonding atoms out of an inert matrix. Instead, it shows the following regular features.

1. The differential gas release rates peak at increasing temperatures, from He to Kr and Xe.
2. The Arrhenius trajectories of He, Ne and Ar show a kink around 500 °C, as predicted by the atomistic theory (Lasaga, 1981).
3. The five diffusivities in the intermediate temperature range (500-1100 °C) vary by a factor 3000.
4. The Arrhenius trajectories of Ne, Ar, Kr and Xe, which are well distinct below 1100 °C, merge above ca. 1300 °C. This requires a major difference in the degassing mechanism.
5. The release of Kr and Xe only sets in at very high temperature, accompanying a major disordering of the apatite structure, documented by Raman spectroscopy, X-ray diffraction, and laser ablation compositional analysis.
6. In addition to the very immobile Kr and Xe, also Ne and Ar are only completely released when the host mineral is completely recrystallized.

Acknowledgements

The Durango apatite samples were donated by Pieter Vermeesch. Valentina Barberini helped with the rare gas laboratory maintenance.

References

Andò, S., Garzanti, E., 2013. Raman spectroscopy in heavy-mineral studies. In: Scott, R., Smyth, H., Morton, A., Richardson, N. (eds.) Sediment Provenance Studies in Hydrocarbon Exploration and Production. Geological Society of London Special Publications, 386, 395-412.

Bhatnagar, V.M., 1969. The melting points of synthetic apatites. Mineralogical Magazine, 37, 527-528.

Capitani, G., Schingaro, E., Lacalamita, M., Mesto, E, Scordari, F., 2016. Structural anomalies in tobelite-2M2 explained by high resolution and analytical electron microscopy. Mineralogical Magazine, 80, 143-156.

Cherniak, D.J., Hanchar, J.M., Watson, E.B., 1997a. Rare-earth diffusion in zircon. Chemical Geology, 134, 289-301.

Cherniak, D.J., Hanchar, J.M., Watson, E.B., 1997b. Diffusion of tetravalent cations in zircon. Contributions to Mineralogy and Petrology, 127, 383-390.

Farley, K.A., 2000. Helium diffusion from apatite: general behavior as illustrated by Durango fluorapatite. Journal of Geophysical Research, 105, 2903–2914.

Ferraris, C., White, T.J., Plévert, J., Wegner, R., 2005. Nanometric modulation in apatite. Physics and Chemistry of

Minerals, 32, 485-492.
Gautheron, C., Djimbi, D.M., Roques, J., Balout, H., Ketcham, R.A., Simoni, E., Pik, R., Seydoux-Guillaume, A.-M., Tassan-Got, L., 2020. A multi-method, multi-scale theoretical study of He and Ne diffusion in zircon. Geochimica et Cosmochimica Acta 268 (2020) 348–367
Gerin, C., Gautheron, C., Oliviero, E., Bachelet, C., Djimbi, M.D., Seydoux-Guillaume, A.M., Tassan-Got, L., Sarda, P., Roques, J., Garrido, F., 2017. Influence of vacancy damage on He diffusion in apatite, investigated at atomic to mineralogical scales. Geochimica et Cosmochimica Acta, 197, 87–103.
Hasebe, N., Barbarand, J., Jarvis, K., Carter, A., Hurford, A.J., 2004. Apatite fission-track chronometry using laser ablation ICP-MS. Chemical Geology, 207, 135-145.
Hetherington, C.J., Villa, I.M., 2007. Barium silicates of the Berisal Complex, Switzerland: A study in geochronology and rare-gas release systematics. Geochim. Cosmochim. Acta 71, 3336-3347.
Kung, J., Villa, I.M., 2021. The *in vacuo* release of Ar from minerals: 2. The role of structural modifications of K-feldspar during heating revealed by Raman microprobe analyses. Chemical Geology, 580, 120382.
Lasaga, A.C., 1981. The atomistic basis of kinetics: defects in minerals. Reviews in Mineralogy, 8, 261-319.
Marks, M.A.W., Wenzel, T., Whitehouse, M.J., Loose, M., Zack, T., Barth, M., Worgard, L., Krasz, V., Eby, G.N., Stosnach, H., Markl, G., 2012. The volatile inventory (F, Cl, Br, S, C) of magmatic apatite: An integrated analytical approach. Chemical Geology, 291, 241-255.
McDowell, F.W., 1983. K-Ar dating: incomplete extraction of radiogenic argon from alkali feldspar. Chemical Geology, 41, 119-126.
Onstott, T.C., Miller, M.L., Ewing, R.C., Arnold, G.W., Walsh, D.S., 1995. Recoil refinements: Implications for the $^{40}Ar/^{39}Ar$ dating technique. Geochimica et Cosmochimica Acta, 59, 1821-1834.
Panzarini, G., Colombo, L., 1994a. Hydrogen diffusion in silicon from tight-binding molecular dynamics. Phys. Rev. Lett., 73, 1636–1639.
Villa, I.M., 2021. The *in vacuo* release of Ar from minerals: 1. hydrous minerals. Chemical Geology, 564, 120076.
Willett, C.D., Fox, M., Shuster, D.L., 2017. A helium-based model for the effects of radiation damage annealing on helium diffusion kinetics in apatite. Earth and Planetary Science Letters, 477, 195-204.
Wolf, R., Farley, K.A., Silver, L.T., 1996. Helium diffusion and low-temperature thermochronometry of apatite. Geochimica et Cosmochimica Acta, 60, 4231-4240.
Wudarska, A., Słaby, E., Wiedenbeck, M., Barnes, J.D., Bonifacie, M., Sturchio, N.C., Bardoux, G., Couffignal, F., Glodny, J., Heraty, L., John, T., Kusebauch, C., Mayanna, S., Wilke, F.D.H., Deput, E., 2021. Inter-laboratory characterisation of apatite reference materials for chlorine isotope analysis. Geostandards and Geoanalytical Research, 45, 121-142.

Figure Captions

Fig. 1 - He degassing rate of Durango apatite. (a) Arrhenius diagram of the present experiment (crosses) and of the literature results of Wolf et al. (1996), displayed as a steep low-temperature array (open circles) and shallower high-temperature array (filled triangles). (b) Arrhenius diagram of the irradiated and the unirradiated aliquots. In the temperature range 500-1100 °C (*i.e.* for $0.73 < x < 1.3$) the two aliquots are indistinguishable.

Fig. 2 - Halogen-derived Ne and Ar degassing rate. (a) Differential release plot. The ordinate axis is the differential gas release in a given step, divided by the temperature difference to the previous step and the square root of the duration of that step. He, solid line; Ne, dashed line; $^{38}Ar_{Cl}$, dotted line; $^{37}Ar_{Ca}$, dash-dotted line. The release of the two Ar isotopes is identical over practically the entire temperature interval. (b) Arrhenius diagram. He, filled circles; ^{20}Ne, open circles; $^{38}Ar_{Cl}$, open triangles; $^{37}Ar_{Ca}$, filled triangles. The fit line to the He data of the irradiated aliquot, from Fig. 1b, is repeated here. The Arrhenius trajectory of Ne is parallel to the He trajectory, shifted by an average factor 7.5 towards lower diffusivity. The trajectory of $^{38}Ar_{Cl}$ also has a slope compatible with the He activation energy, 57 kJ/mol (dashed reference line). The trajectory of $^{37}Ar_{Ca}$ deviates from that of $^{38}Ar_{Cl}$ at T < 780 °C and then merges with it.

Fig. 3 - Reactor-produced Kr and Xe degassing rate. (a) Differential release plot. $^{80}Kr_{Br}$, dashed line; $^{128}Xe_{I}$, dotted line; $^{131}Xe_{Ba}$, long-dashed line; $^{37}Ar_{Ca}$, solid line, for comparison with Fig. 2a. (b) Arrhenius diagram. $^{80}Kr_{Br}$, diamonds; $^{128}Xe_{I}$, squares; $^{131}Xe_{Ba}$, crosses. The points below 1300 °C are hardly meaningful, as the neutron-produced isotopes are calculated after subtraction of atmospheric contribution and have a high uncertainty (especially Xe). What is very robust is the massive break in slope at 1300 °C.

Fig. 4 - Raman spectroscopy results on Fragment C before and after stepheating. (a) Principal apatite vibration mode (964 cm^{-1}). The sharpness has drastically decreased upon heating. (b) Color-coded Raman map (ca. 1.8x0.7 mm) obtained in a corner of Fragment C. The heterogeneity of the unheated sample is smoothed away by heating.

Fig. 5 - X-ray diffraction of Fragment C before and after stepheating.

Supplementary Materials

Table S1 - rare gas results

Figure

Click here to access/download;Figure;Villa-Fig1.pdf

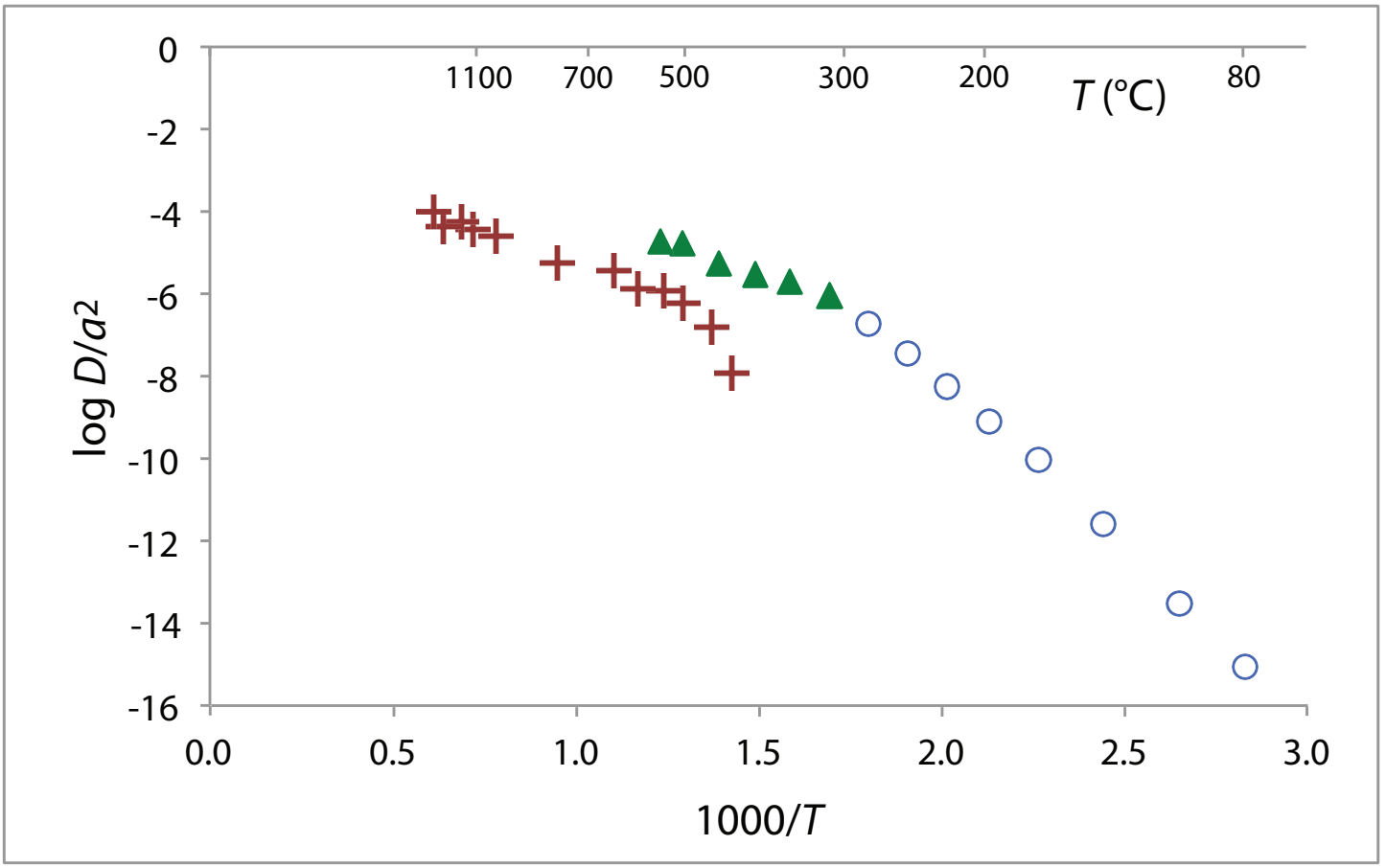

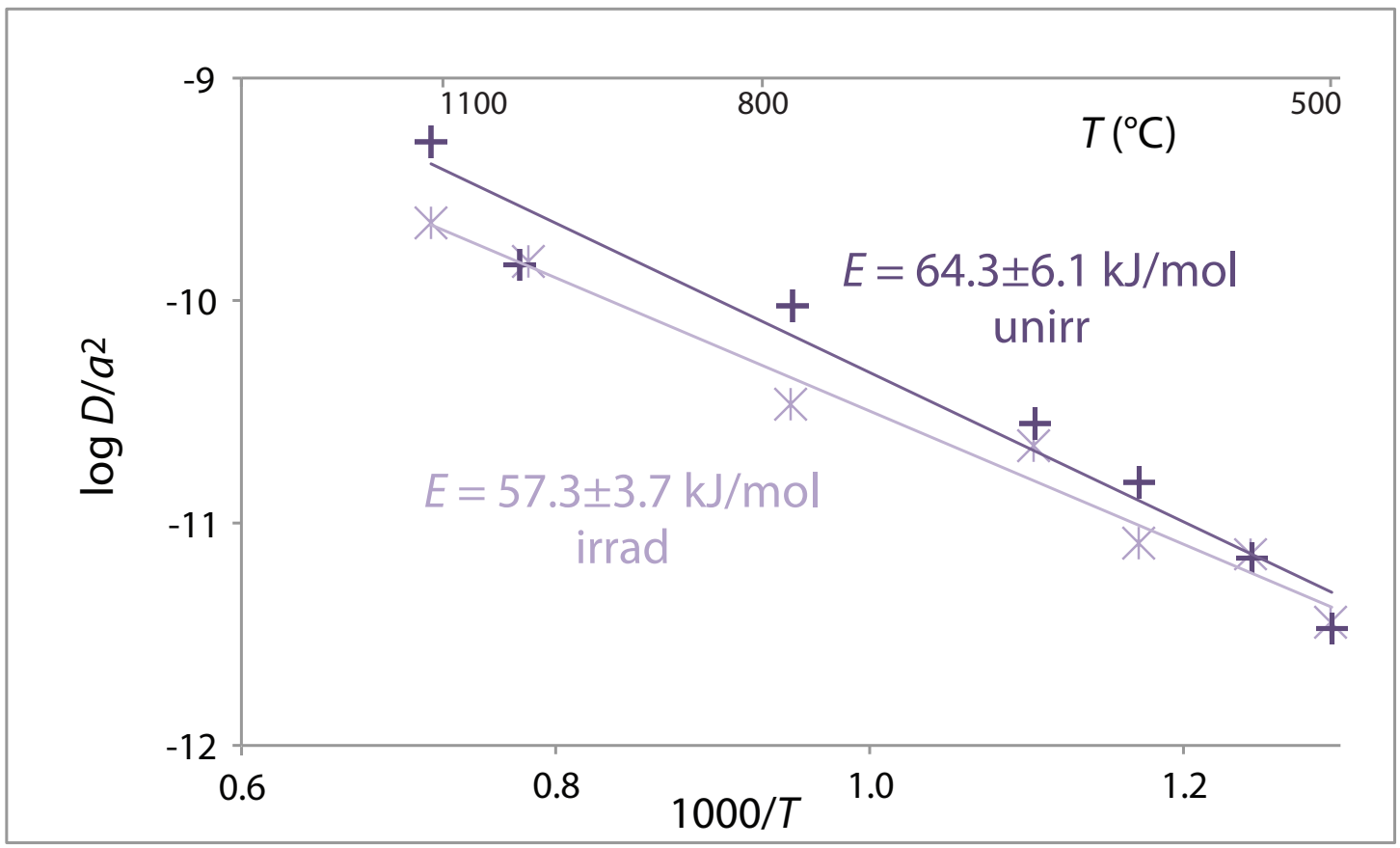

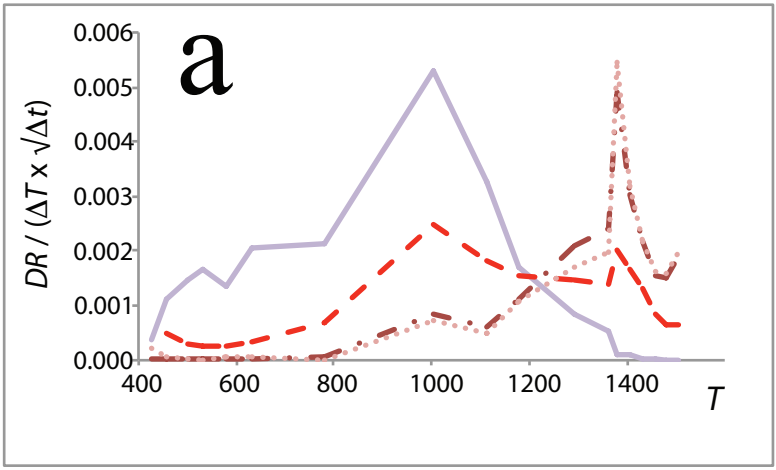

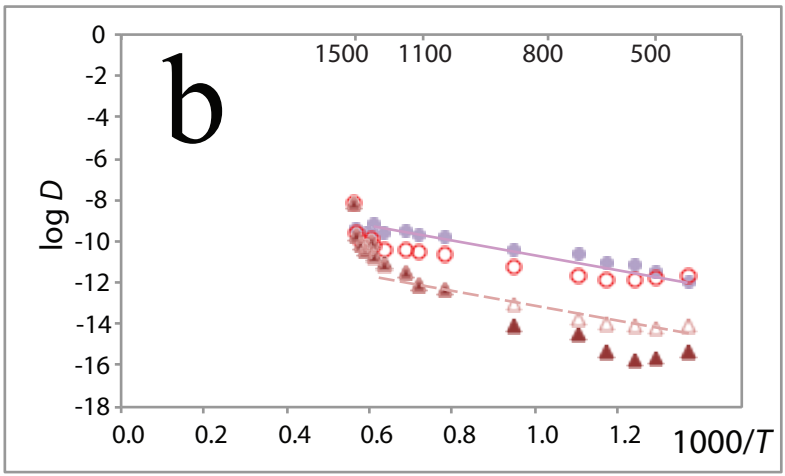

Villa et al Fig. 2

Figure

Click here to access/download;Figure;Villa-

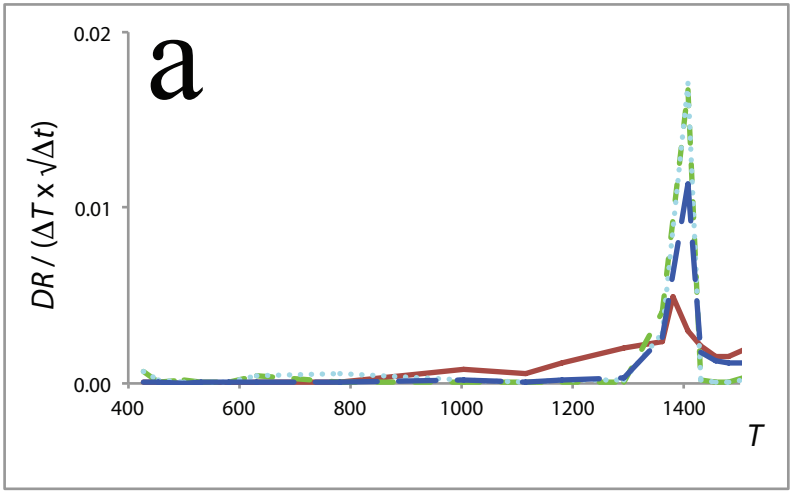

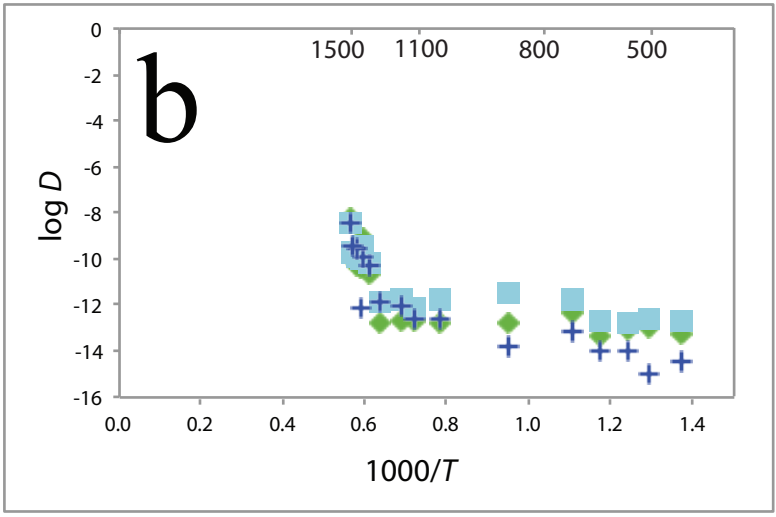

Villa et al Fig. 3

Figure

Click here to access/download;Figure;Villa-Fig4.pdf

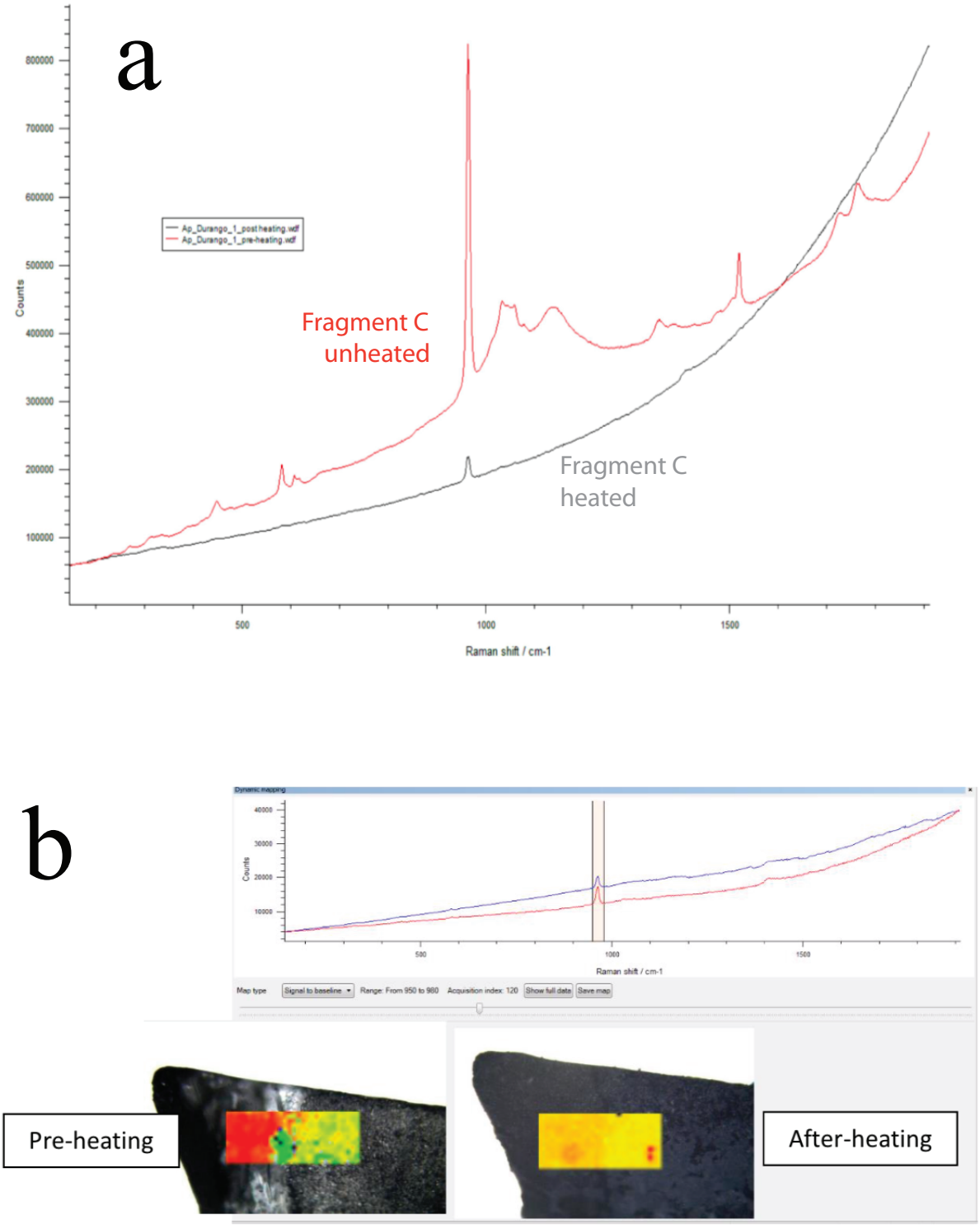

Villa et al Fig. 4

Figure

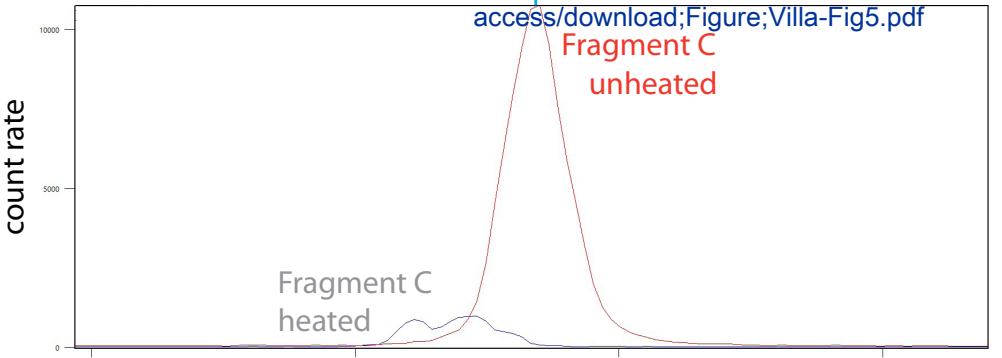
Apatite peak position
Click here to access/download;Figure;Villa-Fig5.pdf
Fragment C unheated
Fragment C heated
count rate
10000
5000
0
25°
25.5°
26°
2θ angle
26.5°

Supplementary file

Click here to access/download

Supplementary file

Villa-SupplemTable.xlsx